Tailoring the Film Morphology and Interface Band Offset of Caesium Bismuth Iodide based Pb Free Perovskite Solar Cells

Dhruba B. Khadka‡†*, Yasuhiro Shirai†*, Masatoshi Yanagida† and Kenjiro Miyano†

‡ International Center for Young Scientists (ICYS), National Institute for Materials Science (NIMS), 1-1 Namiki, Tsukuba, Ibaraki 305-0044, Japan.

†Global Research Center for Environment and Energy based on Nanomaterials Science (GREEN), National Institute for Materials Science (NIMS), 1-1 Namiki, Tsukuba, Ibaraki 305-0044, Japan.

Corresponding Author

*E-mail: KHADKA.B.Dhruba@nims.go.jp

*E-mail: SHIRAI.Yasuhiro@nims.go.jp

ABSTRACT

The bismuth-based halide perovskites (Bi-HaP) are low toxic and air stable materials with promising photo-absorber properties. In this work, we have fabricated the Bi-HaP ($Cs_3Bi_2I_9$, $CsBi_3I_{10}$) film by solution process followed by solvent annealing and investigated the crystal growth and optoelectronic properties of those materials. A compact and large grain morphology of Bi-HaP films have realized by annealing under ambient solvent vapor. A collective analysis of XRD patterns, Raman spectra, absorption, and PL spectra of fabricated films corroborates that the $Cs_3Bi_2I_9$ film (E_g~ 2.08 eV) of the hexagonal crystal phase is stable under annealing at wide temperature range and ambient solvent vapor annealing compared to another $CsBi_3I_{10}$ thin film having narrower E_g~ 1.8 eV of Bi-HaP family. We have achieved the best power conversion efficiency of ~1.26% with an open circuit voltage of 0.74 V for the device with $Cs_3Bi_2I_9$. The analysis of materials properties and device characteristics indicates that the morphology tailoring, control of surface chemistry coupled with interface band offset engineering are important for further improvement of the Bi-HaP based device.

Keywords: Bi based perovskite, Pb free, crystallinity, interface, optoelectronic properties

1. Introduction

Lead halide perovskite (Pb-HaP) has emerged as a promising photo-absorber material demonstrating competitive power conversion efficiency (*PCE*) to other PV technologies.[1] However, there are some fundamental issues associated with Pb-HaP PV devices; (a) instability under ambient air [2,3](b) presence of a heavy toxic element (Pb)[4,5] for commercialization.[6] It is therefore important to explore nontoxic and stable perovskite-based alternative materials. As akin of the Pb-HaP, Sn and Ge based HaP materials have been explored for the replacement of the Pb based perovskite.[7,8] However, unstable +2 oxidation states of Sn and Ge are easily oxidized to +4 states due to lack of the inert pair effect as in Pb^{2+} ions which are deleterious for getting the high quality film, device performance, and stability.[9–11]

On the surge of alternatives, Bi and Sb-based perovskite materials have been extensively investigating as possible candidates due to their promising opto-physical properties and the superior stability in ambient air.[12–18] The multiple groups suggested that the poor morphology of the fabricated film is a big hurdle for the poor device performance.[19–21] Johansson and co-workers studied the photovoltaic characteristics of $A_3Bi_2I_9$ using single step spin coating on mesoporous TiO_2.[12] Ran et al. employed two-step deposition technique by evaporating BiI_3 followed by spin coating with methylammonium iodide (MAI) to fabricate a compact film.[22] Some groups[19,20] reported the solvent-engineering or solvent assisted crystallization approaches for the improvement in film morphology. A recent work by Zhang and co-workers[23] have demonstrated a remarkable improvement in device performance using ultrathin $Cs_3Bi_2I_9$ nanosheets in n-i-p device structure tuning with the hole transport layer. The device with $MA_3Bi_2I_9$ material has also been explored to improve the device performance by tailoring the morphology and carrier transport engineering.[24–26] Despite the superior stability in ambient atmosphere,[27] the poor device performance is very disappointing. Since the plethora of research works have been focused on Pb-HaP devices,[28] the reports on the fundamental understanding

of the Bi-HaP materials are lacking. Therefore, it is imperative to have an extensive exploration of the crystal growth, morphology and optoelectronic properties of Bi-HaP to disentangle the limiting factors of device parameters for this class of materials.

In this study, we have investigated the film growth, structural and optophysical properties of the bismuth Caesium halide perovskite (CBI) ($CsBi_3I_{10}$ (CBI-1) and $Cs_3Bi_2I_9$ (CBI-2)) deposited by solution process for the solar cell application. It is found that the CBI-2 film has a stable single phase under the growth of wide range temperature. We have obtained a large gain film morphology by solvent dripping subsequent with solvent annealing during crystallization. We have demonstrated the inverted CBI-2 device of the best power conversion efficiency (*PCE*) ~ 1.26%. This is mainly attributed by improving the film quality (surface morphology, control of trace of metallic content) and interface band offset. We have explored the limiting factors behind the poor performance of the CBI absorber layer and pave the way for the improvement in device properties.

2. Results and Discussion

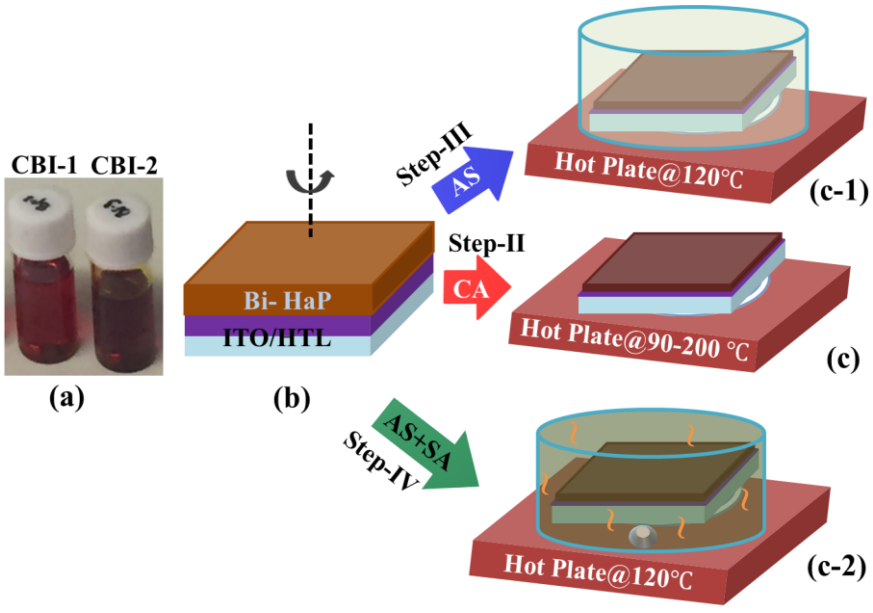

Fig. 1. Schematic of the fabrication approach of the Bi-HaP thin film. (a) Precursor solutions of CBI-1 and CBI-2, (b) deposition of the film on the ITO/HTL substrate. The crystallization of as spin coated films; (c) conventional annealing (CA) at various temperatures, (c-1)

annealing the antisolvent (chlorobenzene) dripped film at 120 ℃ denoted as AS, (c-2) annealing the antisolvent dripped film under ambient dimethylformamide (DMF) vapor at 120 ℃ termed as AS+SA.

The Bi-HaP thin films were fabricated by solution approach as depicted in Fig. 1. To understand the film growth, we initially prepared the Bi-HaP films of two compositions ($CsBi_3I_{10}$ (CBI-1) and $Cs_3Bi_2I_9$ (CBI-2)) by conventional annealing (CA) as shown in Fig. 1c. Figure 2 displays the morphology, structure and opto-physical properties of respective films. The SEM images of both (Fig. 2a, b) demonstrate comparatively rough morphology. The morphology of the CBI-1 film exhibits small granular crystal while that for the CBI-2 film consists of large grain with the flake-like feature which is alike to the reports.[12,13] The XRD pattern for CBI-1 (Fig. 2c) with dominant peak of (003) orientation along with (113) and (300) having very similar crystal orientations to the BiI_3 crystal of rhombohedral phase which is consistent with the report by Johansson et al.[13] It is suggested that CBI-1 possesses a layered structure alike to BiI_3 but these layers are partly broken into the zero-dimensional structure as in CBI-2. The CBI-2 film has crystal growth with the most significant peak intensity at (006) orientation (Fig. 2c) of the hexagonal phase.[14,19] Since the XRD patterns are not so sensitive for detection of impurities in the film. We have measured the Raman spectra (Fig. 2d) for further confirmation of crystal quality. The Raman spectrum of the CBI-1 film exhibits characteristic peaks at 62, 104 and 146 cm^{-1}. Similarly, the characteristic Raman peaks for the CBI-2 film are assigned at 62, 92, 104, and 146 cm^{-1}. We also examined Raman spectra of the BiI_3 film which have the characteristic peaks at 71, 84, 112, and 158 cm^{-1}. These results are in agreement with the theoretical and experiment reports.[29–31] Since the Raman peak at 112 cm^{-1} (A_g)[30] is the main characteristic peak of BiI_3 which cannot be excluded in the Bi-HaP film under such a broad peak in Raman spectra. In addition, the CBI-1 and CBI-2 films assign very close characteristic peaks, so it is complicated to rule out the presence of those phases in either film.

Further studies are required to elucidate the existence of secondary phases and their impacts on film quality.

Figure 2e reveals the absorption spectra of the respective films. The CBI-1 film having brown blackish color exhibits band gap energy (E_g)~ 1.80 eV (690 nm) along with additional exciton absorption peak at ~2.53 eV. On the other hand, the CBI-2 film having orange-red color depicts E_g ~ 2.08 eV (598 nm) with additional exciton absorption peaks at 2.53 and 2.95 eV. The PL spectra (Fig. 2f) show peak centered at ~1.80 eV for the CBI-1 film and ~ 2.08 eV for the CBI-2 film. These results are in good agreement with the reports.[13,32] Although the absorption spectra for the CBI-1 film possesses an additional slope with the intercept at ~1.95 eV, no such additional feature was noticed in PL spectra. Note that the absorption and PL spectra of BiI_3 thin film have shown close features as observed in the other report.[33] Moreover, we observed a set of parasitic PL peaks at the lower energy regime. This is suggested as an indication of cascade excitations showing the possibility of the re-absorption and re-emission of photons in the micro-scale crystals. Irvine and co-workers[34] reported that the Bi-HaP film has highly anisotropic photoluminescence emission and excitation as a consequence of the large proportion of localized excitons coupled with delocalized excitons from intercluster energy transfer.

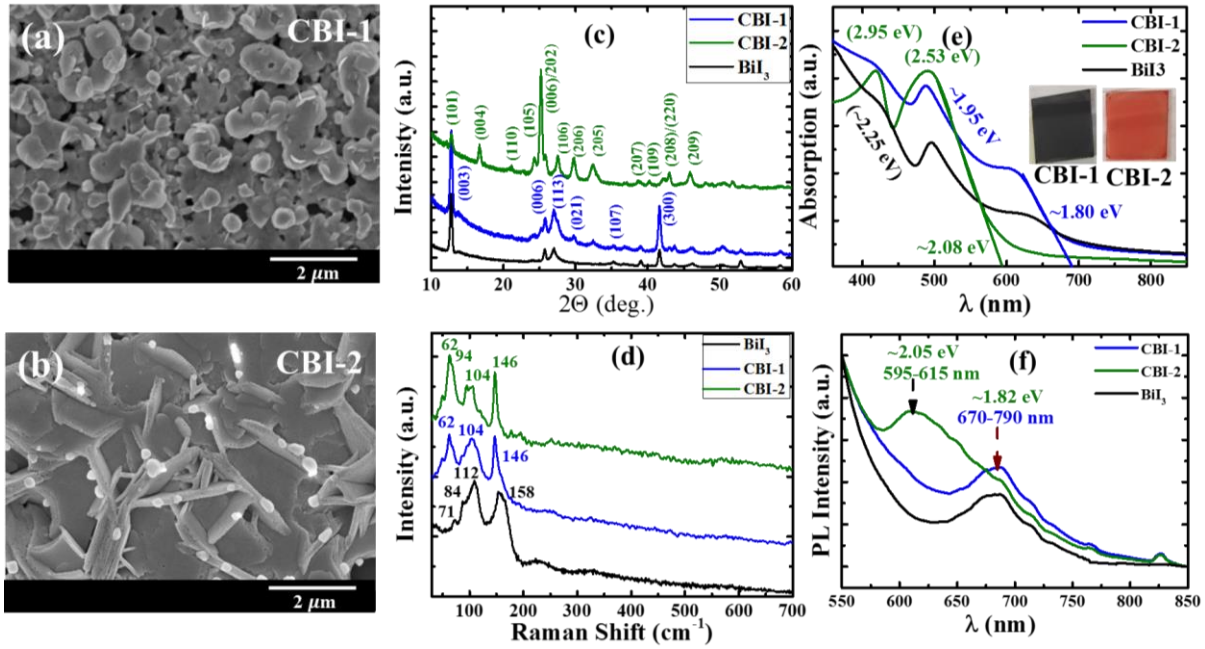

Fig. 2. SEM images of CBI-1 (a) and CBI-2 (b) thin films, (c) XRD patterns, (d) Raman spectra, (e) absorption spectra, and (f) PL spectra of the respective films. Inset in Fig. e shows the photographs of the CBI-1 and CBI-2 films.

To investigate the effect of annealing temperature on the structural and optophysical properties of the Bi-HaP films, we fabricated the thin films annealed by varying temperatures from 90-200 ℃. Interestingly, the CBI-2 film shows almost identical XRD, Raman and PL spectra (Fig. S1, supporting information) annealing at temperature 90- 200 ℃. To have a distinct comparison, we have plotted the XRD patterns and PL spectra at 120 and 200 ℃ as depicted in Fig. 3. For the CBI-1 film, the XRD patterns, Raman and PL spectra exhibit identical characteristics of the films annealed at 90- 180 ℃ but that of annealing at 200 ℃ shows characteristics features alike to the CBI-2 film whereas the CBI-2 film is found to be thermally stable. One can also see a clear difference in the photograph (Inset in Fig. 3 a, b and Fig. S1a, Supporting Information). It is speculated that the $CsBi_3I_{10}$ decomposes into $Cs_3Bi_2I_9$ and BiI_3 along with by-products; metallic bismuth and Iodine during. The decomposition route is proposed as below.

$$3CsBi_3I_{10}\,(s) \rightarrow Cs_3Bi_2I_9\,(s) + 7BiI_3\,(s) \qquad (1)$$

$2BiI_3\,(s) \rightarrow 2Bi\,(s) + 3I_2\,(g)\uparrow$ (2)

Note that the formation of $Cs_3Bi_2I_9$ (s) in reaction (1) results in the red appearance of the film. It is substantiated by XRD and PL characteristics as depicted in Fig. 3. The existence of metallic Bi (as shown in reaction (2)) has been detected in the CBI-1 film (from XPS analysis will be discussed in succeeding paragraph) which supports decomposition of BiI_3. We found that the Bi-HaP films annealed at 120 ℃ have rather better crystallinity and morphology. The film annealed at 90 ℃ is comparatively poor for both films and annealing above 180 ℃ also worsens the film morphology. Furthermore, to confirm the film stability, we examine the Bi-HaP film stored in ambient air for more than six months. The XRD patterns of aged and fresh films (Fig. S2, Supporting Information) do not show any change for both which ascertains the film stability under ambient air. This is important for device stability.

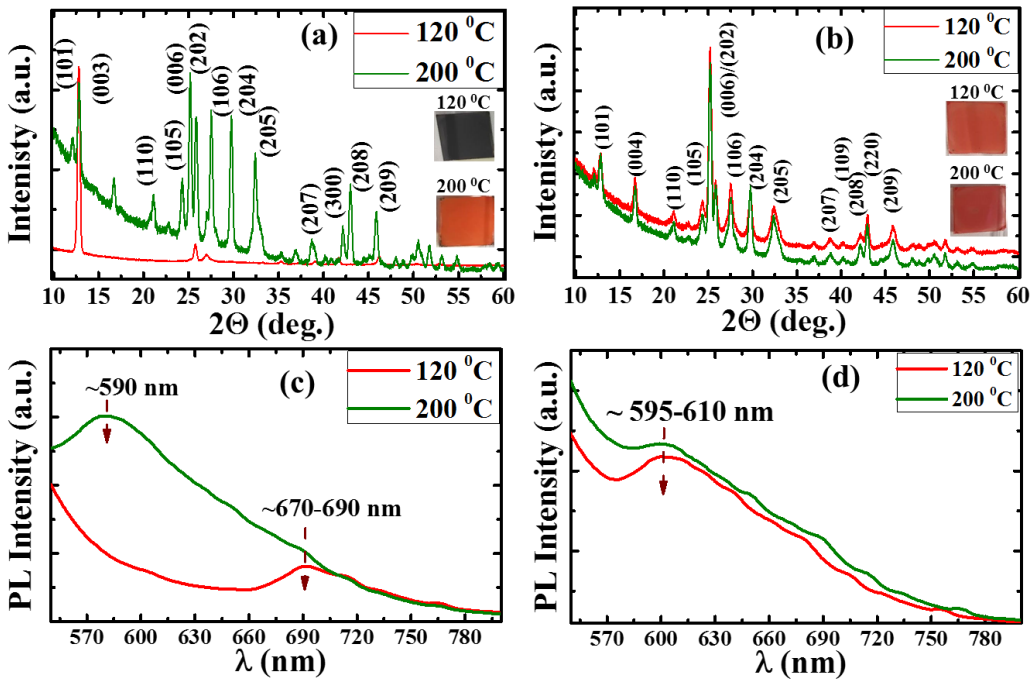

Fig. 3. XRD patterns of the CBI-1 (a) and CBI-2 (b) thin film annealed at 120 and 200 ℃ and PL spectra (c, d) of the respective thin films.

After investigating the material growth of the Bi-HaP films, we prepared a complete device of inverted configuration as depicted in Fig. 4a. The *J-V* curves (Fig. 4b) demonstrate the device

with Bi-HaP films prepared by the CA method. The device with CBI-2 has poor device efficiency with diode curve while that for the CBI-1 film is much worse. This is primarily attributed to the poor morphology of the CBI-1 film compared to the CBI-2 film. Therefore, it is exigent to improve the film morphology for the enhancement in device performance.

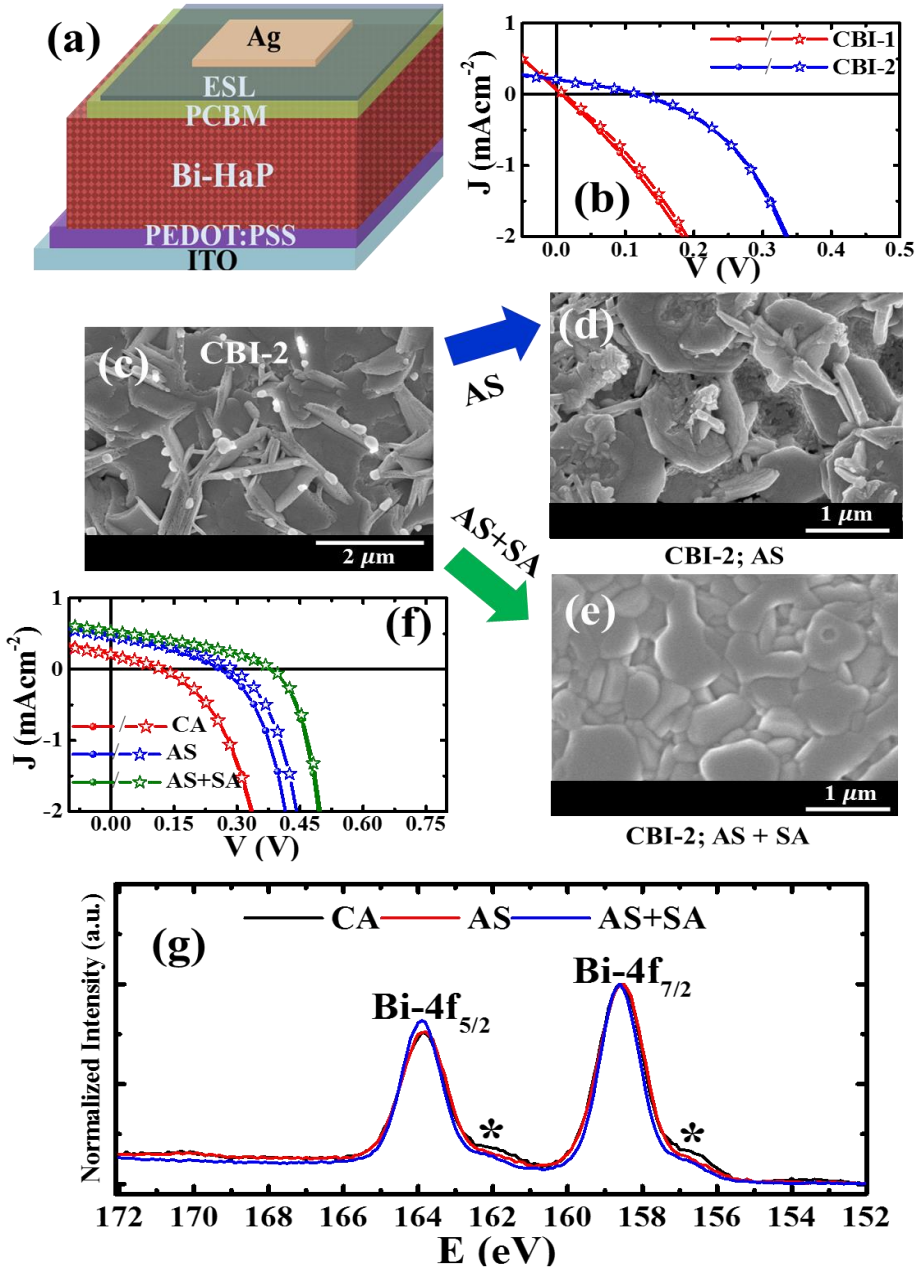

Fig. 4. Schematics of device configuration (a), *J-V* characteristics of device with Bi-HaP films (CBI-1 and CBI-2) prepared by CA (b), SEM images of CBI-2 films fabricated at different conditions; (c) CA, (d) antisolvent (AS) dripping, (e) antisolvent dripping subsequent with annealing under solvent vapor (AS+SA) and (f) *J-V* characteristics of the device using CBI-2

films (a, b, c) with PEDOT:PSS as an HTL. Here, the symbols in *J-V* curves stand for forward and reverse scan direction. The XPS spectra of CBI-2 film (prepared by CA, AS, AS+SA) assigned for the core-level peak of Bi-4f ((g). The two steric signs at ~162 and 157 eV indicate for the metallic Bi^0.

In order to tailor the film morphology, we prepared the films using antisolvent (AS) and subsequent with ambient solvent vapor annealing (AS+SA) method as depicted in Fig. 1 (c-1 and c-2). This approach dramatically improved the film texture for CBI-2 film as depicted in Fig. 4c-d. The morphology of CBI-2 film is found to be compact and more uniform with antisolvent dripping followed by ambient solvent vapor annealing. The XRD patterns (Fig. S3b, Supporting Information) also exhibited the intensified characteristics peaks suggesting a better crystal quality. Interestingly, the XRD patterns (Fig. S3a, Supporting Information) for CBI-1 films (CA and AS) are similar while that for the CBI-1 film treated with AS + SA assigned a contrast XRD pattern with a dominant peak of (113) orientation with other peaks of (003) and (205). In our work, we found that the Bi-HaP film is much sensitive under ambient solvent vapor annealing. We must have well-controlled ambient DMF solvent vapor annealing for crystallization. Similarly, unlike to our expectation, the surface texture of CBI-1 films (Fig. S4, Supporting Information) is not improved distinctly. However, we see comparatively uniform grain for the film prepared with chlorobenzene dripping while that for the films with CA and AS+SA are almost alike in appearance. Moreover, the surface texture of the CBI-1 film contains small flake-like features as observed in the CBI-2 film and small granular feature as in the BiI_3 film (Fig. S5a, Supporting Information). Interestingly, we observed that the antisolvent treatment and ambient solvent vapor annealing distinctly affect on the growth of Bi-HaP films (CBI-1 and CBI-2). Buonassisi and co-workers[19] have discussed the film formation mechanism of Bi-HaP based perovskite by the solvent-engineering method. It is suggested that the precursor supersaturation affects the grain nucleation and growth which determine the morphology of Bi-HaP film. Note that the antisolvent dripping rapidly increases

homogeneous nucleation resulting in a compact film with smaller grains. In our work, we have annealed the antisolvent dripped CBI-2 film under slow evaporation rate covering by a petri dish (as depicted in Fig. 1c-1) which prolongs the crystallization process (grain nucleation) and results in larger and homogeneous grain (Fig. 4d). Similarly, as the antisolvent dripped CBI-2 film is annealed under controlled ambient DMF vapor covering by petri dish (Fig. 1c-2), it further prolongs the crystallization process and hence a compact film with homogeneous and large grains (Fig. 4e) is formed. In case of the CBI-1 film, the precursor ($CsBi_3I_{10}$; CsI:BiI3::1:3) consists of the BiI_3 rich composition. It has been reported that the DMF or dimethyl sulfoxide (DMSO) solvent forms bismuth complexes with BiI_3 which affects the precursor supersaturation level and film formation.[19] Therefore, when we annealed the CBI-1 film under the ambient DMF vapor, it may affect the supersaturation level on the pre-crystallization stage of film growth as a consequence of BiI_3 rich composition which hinders the nucleation of grain and hence results in a poor film morphology. The detail discussion on the film formation mechanism is beyond the scope of this work.

To evaluate the impact of morphology on the device, we fabricated the device with CBI films with PEDOT:PSS as HTL coupled with PCBM as ETL. Unlike to our expectation, the *J-V* curves (Fig. S4b) of CBI-1 films prepared by AS and AS+SA method are not improved. This must be due to the consequence of the poor film morphology or the existence of a trace of secondary phase in it. Since CBI-1 film has seminal characteristics to the BiI_3 film, the BiI_3 material also has been reported for the solar cell application.[35,36] Here, we also prepared BiI_3 film with chlorobenzene dripping. Interesting, the film morphology of BiI_3 is rather uniform and compacts (Fig. S5a, Supporting Information), the device with bismuth trihalide (BiI_3) film (Fig. S5b) demonstrated a better *J-V* characteristic. It conjectures that the poor film quality or surface chemistry might be detrimental for the device with CBI-1 film. Figure 4f shows the *J-V* curves of devices with the CBI-2 films prepared by different annealing approaches (CA, AS,

and AS+SA). The device parameters (Table 1); J_{SC}, V_{OC}, and *FF* are noticeably improved compared to that of the device with CBI-1 film which is mainly attributed to the surface morphology tailoring of the CBI-2 film (Fig. 4c-e). Our results agree with the reports on the Bi-HaP based solar cells.[19,22] It has been documented that the large and uniform gain has a low grain boundary density which reduces the recombination centers.[37]

Furthermore, we explored the Bi-HaP film by X-ray photoelectron spectroscopy (XPS) analysis to dig up the surface chemistry of the films. The XPS core-level spectra (Fig. S6; Supporting Information) display the characteristics signal from the Cs-3d, Bi-4f, and I-3d electronic states. The XPS characteristics peaks for Cs-3d and I-3d are alike for both films. But the shoulder peaks at ~162 and 157 eV are detected in the core-level signal for Bi-4f in the CBI-1 film which is much low in the CBI-2 film. These peaks correspond to the metallic Bi^0 [14] which could be due to the decomposition of caesium bismuth iodide and bismuth triiodide during annealing as discussed above (reaction (1) and reaction (2)). It is presumed that the volatility of BiI_3 results in iodine deficient stoichiometry and a trace of metallic Bi^0 state remains.[14] Note that a trace of metallic Bi^0 on the Bi-HaP film is notorious for recombination centers and Fermi level pinning which deteriorates the device performance. Thus, it is speculated that the surface with a trace metallic state could be one of the detrimental factors for the poor performance of the device with the CBI-1 film compared to the CBI-2 device. In the case of the CBI-2 film as displayed in Fig. 4g, although a lower characteristic peak of metallic Bi^0 exists in the film prepared by CA, it is significantly diminished in the CBI-2 film prepared by a controlled process (AS and AS+SA). This also supports the results of the devices with CBI-2 (Fig. 4f and Table 1). This result indicates that the film morphology, as well as the surface chemistry, are very critical for the improvement of the device performance.

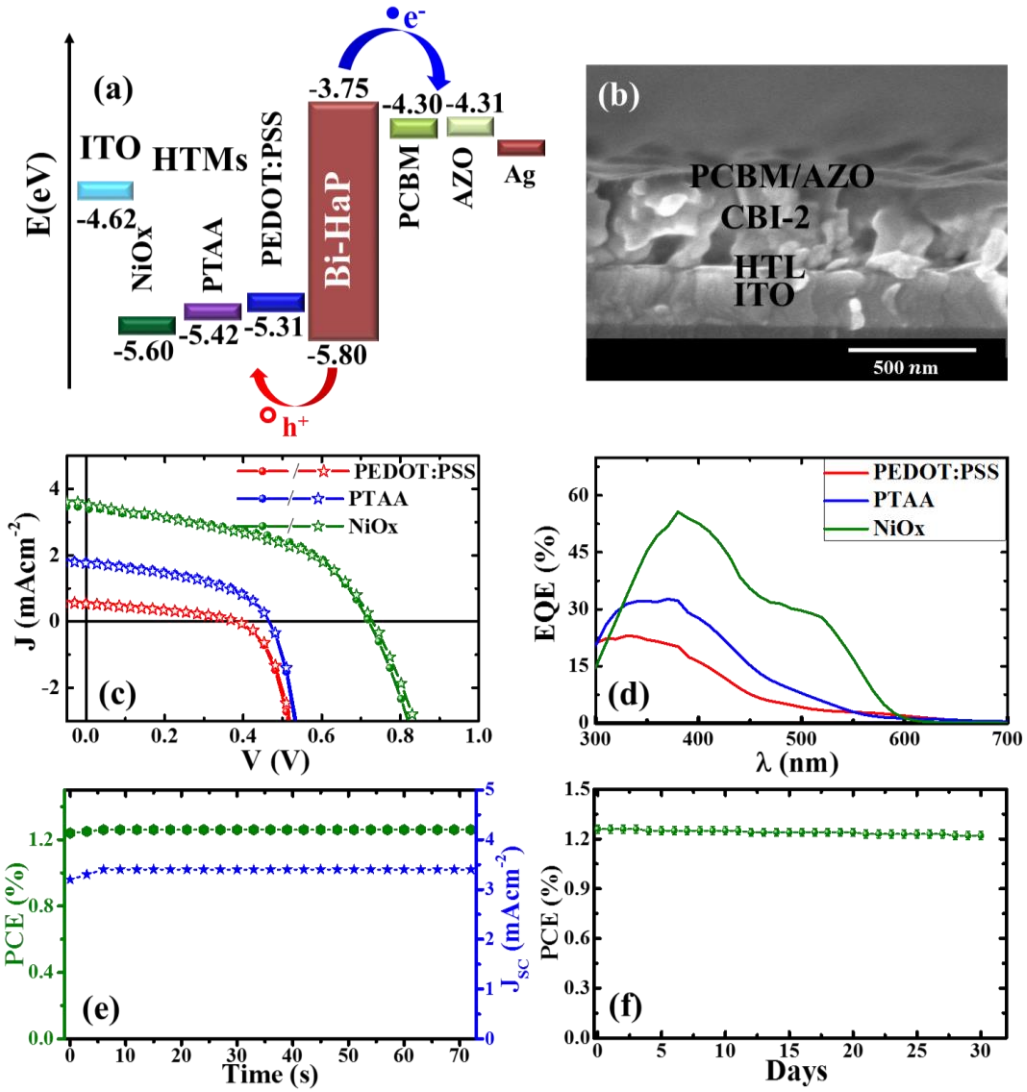

Fig. 5. (a) Schematic of the energy band diagram, (b) cross-sectional images of typical Bi-HaP (CBI-2) solar cells. (c) *J-V* curves of CBI-2 devices with different HTLs; PEDOT:PSS, PTAA, and NiO_x, (d) *EQE* spectra of corresponding devices. (e) Steady-state JSC and PCE of CBI-2 device with NiOx at maximum power point tracking (MPPT) under AM 1.5G 100 $mWcm^{-2}$ illumination and (f) stability of the device stored in ambient air conditions.

Table 1. The figure of merits of Bi-HaP device with CBI-2 thin film fabricated by various methods; CA, AS, AS+SA and with different HTLs. J_{SC}: short circuit current density, V_{OC}: open circuit voltage, *FF*: fill factor, η: power conversion efficiency. The best device parameters are given outside the parentheses. The figures of merit given in the parentheses consist the average values and standard deviation (15 devices from 3 batches)

Device Parameters	Morphology tailoring			Interface engineering (AS+SA)		
	CA	AS	AS+SA	PEDOT:PSS	PTAA	NiOx
J_{sc} ($mAcm^{-2}$)	0.21 (0.17±0.05)	0.46 (0.44±0.07)	0.54 (0.52±0.04)	0.54 (0.52±0.04)	1.76 (1.72±0.07)	3.42 (3.38±0.03)
V_{OC} (V)	0.12 (0.08±0.03)	0.29 (0.25±0.05)	0.38 (0.36±0.03)	0.38 (0.36±0.03)	0.47 (0.43±0.04)	0.74 (0.72±0.03)
FF	0.29 (0.26±0.05)	0.34 (0.31±0.05)	0.35 (0.33±0.02)	0.35 (0.33±0.02)	0.45 (0.42±0.03)	0.51 (0.50±0.02)
η (%)	0.0074 (0.0067±0.001)	0.046 (0.042±0.005)	0.073 (0.068±0.005)	0.073 (0.068±0.005)	0.37 (0.31±0.05)	1.26 (1.22±0.04)

Considering the wide band gap of the Bi-HaP materials with deep valence band edge,[14] a poor band alignment at the interface would lead to low device performance by constraining the device parameters. To investigate this issue, we have fabricated the devices with the CBI-2 film (prepared by AS+SA) employing different HTLs as of our experience on the lead halide perovskite based devices.[38,39] Here, we focused only on devices with the CBI-2 film because of better film morphology and surface chemistry as discussed above. Note that the PTAA and NiO_x HTLs were plasma treated prior to deposition of the CBI-2 film on it which is very important to mitigate the non-wettability surface and tuning the HOMO and LUMO level.[40,41] The photoelectron spectra of respective plasma treated PTAA and NiOx films are given in Fig. S7 (supporting information). The energy band alignment is as depicted in Fig. 5a. The cross-sectional image of the typical device (ITO/HTL/CBI-2/PCBM) is given in Fig. 5b. The *J-V* curves show negligible hysteresis (Fig. 5c). The figures of merit (Table1) of the best devices demonstrate a significant improvement in device parameters. The devices with organic HTLs (PEDOT:PSS, PTAA) have a lower device performance than the device with NiOx. Here, we achieved the best device performance with NiOx of ~1.26 % efficiency accompanied by improving V_{OC} (0.742 V), *FF* (0.507), and J_{SC} (3.416 $mAcm^{-2}$). The enhancement in device

parameters is attributed to the better interface quality, improved band alignments, and efficient carrier transport. It is to be noted that the band offset at the Bi-HaP/HTL is diminished with the plasma treated HTL which increases the built in potential as well as improves the interfacial carrier transport and hence enhances the device parameters.[19,40] This work suggests that the optimization on the surface morphology and the interface band offset is very important for further improvement of the Bi-HaP based devices. Figure 5d shows the spectral response (*EQE*) of the respective devices. The integrated J_{SC} estimated from the *EQE* spectra is in agreement with the value obtained from the respective *J-V* curves. One can see a lower and much varied response in the absorption range of the CBI-2 film (~ 400- 600 nm). This is correlated to the kinetically favourable interface barrier, quality of interface and absorber layer. Furthermore, Fig. 5e displays a steady-state photocurrent of ~3.42 $mAcm^{-2}$ over a period of one minute at MPPT under one sun illumination which corresponds to a steady-state PCE of ~1.26% for the CBI-2 device with NiO_x. We also monitored the stability of the device stored in the air under ambient conditions. It demonstrated promising stability as depicted in Fig. 5f which retained over 95% of its original PCE after 30 days. This result clearly demonstrates that the Bi-HaP device is highly stable than the Pb and Sn-based HaP devices.[42] Therefore, it could be a promising alternative of Pb based perovskite device to resolve the toxicity and instability issue if we achieve a competitive performance of the Bi-HaP based perovskite device. Indeed, there is much room to play with the band alignment for favourable carrier kinetics and improvement in film quality of Bi-HaP to get a better device performance.

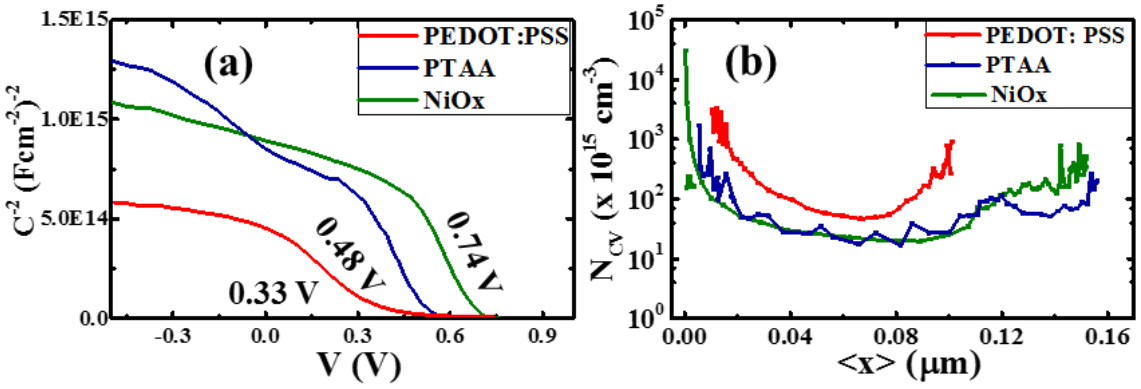

Fig. 6. Mott-Schottky plot (a) and carrier density profile (b) obtained from capacitance- voltage (*C-V*) curves of the Bi-HaP (CBI-2) devices with HTLs; PEDOT:PSS, PTAA and NiOx.

To get further insight, we analyzed the capacitance-voltage data response which is rarely reported for this class of materials. We carried out capacitance-voltage (*C-V*) measurements and extracted the Mott-Schottky plot (Equation 3, Fig. 6a) and carrier profile (Equation 4, Fig. 6b) estimated by the relation,[43]

$$C(V)^{-2} = \frac{2}{q\varepsilon_0\varepsilon_s N_A(x)}(V + V_D) \qquad (3)$$

$$N_A = -\frac{2}{q\varepsilon_0\varepsilon_s A^2}\left[\frac{d}{dV}\left(\frac{1}{C^2}\right)\right]^{-1} \qquad (4)$$

where C is capacitance per area, ε_0 is permittivity of free space, ε_s is a dielectric constant of perovskite layer which is estimated from the plateau region of capacitance-frequency (*C-f*) plot measured at zero bias under dark as mentioned in our earlier reports.[44] V_D is diffusion potential, (given by $V_D = V_{bi} - E_F/q$; where Fermi energy- E_F and built in potential- V_{bi}). N_A is the carrier density corresponding to V_D estimated from the Mott-Schottky (*M-S*). The Mott-Schottky plots (Fig. 6a) show the impacts on diffusion potential (V_D). Note that the V_D is given by relation; $V_D = V_{bi} - E_F/q$; where E_F- Fermi energy and V_{bi} - built in potential. The value of V_D for the PEDOT: PSS device (0.33 V) is lower than the PTAA (0.48 V) and NiOx (0.74 V) devices. This can be partially contributed by more favourable band alignment and the optoelectronic quality of the film grown on the respective substrate. The slanted broader line at M-S plot indicates the p-type doping induced at the

interface. The carrier profile estimated from *C-V* analysis (Fig. 6b) has the higher carrier density for PEDOT:PSS~ $1x10^{17}$ cm^{-3} while that for PTAA and NiOx lies in the range ~3 $x10^{16}$ cm^{-3}. Note that the carrier densities corresponding to the respective HTLs are approximately one order higher than the Pb based HaP devices in our previous reports.[45] It has been reported that the carrier density estimated from *C-V* analysis also have an influence of the trap densities in the absorber layer.[43] The higher carrier densities in our devices could be partially contributed from the trap induced in the Bi-HaP layer during the crystallization. It is noticed that the carrier profiles are slightly confined for the PEDOT:PSS device compared to the other devices. It also shows a narrow space charge region. This might be due to the Bi-HaP/HTL interfacial chemistry at the junction, interface defect and the film quality which indeed are important for device optimization as reported for the Pb-HaP based perovskite device.[46] Therefore, our work suggests that the explorations on many aspects such as; film quality, interface engineering and defect physics of the Bi-HaP material are crucial to open up its potential for getting efficient device performance as well as its applications in other optoelectronics fields.

3. Conclusions

We have demonstrated a solution approach for growing high quality and compact Bi-HaP films by antisolvent dripping followed by solvent annealing. The material growth and optophysical properties of the Bi-HaP ($Cs_3Bi_2I_9$, $CsBi_3I_{10}$) were investigated by XRD patterns, Raman spectra, absorption spectra and PL spectra for its application in the PV device. The $Cs_3Bi_2I_9$ film (E_g~2.08 eV) shows rather high crystallinity (single crystal phase) and compact surface morphology than the $CsBi_3I_{10}$ film (E_g~1.80 eV) and hence the performance of the device with the $Cs_3Bi_2I_9$ film is found to be superior in spite of having a more suitable band gap of the $CsBi_3I_{10}$ film for light harvesting. The performances with devices with $Cs_3Bi_2I_9$ film are enhanced by diminishing the band offset using the PTAA and NiOx having a deeper HOMO

level in place of PEDOT:PSS as HTL. The device with NiO_x as hole transport layer demonstrated the best PCE of 1.26% with V_{OC}~ 0.74 V and J_{SC}~ 3.42 $mAcm^{-2}$ which is competitive to the best reports using Bi-HaP absorber layer. This is attributed mainly to the improved surface morphology, reduced interface energy barrier and increase in diffusion potential. This work paves the way of getting high performance of the Bi-HaP based device by further the control of surface morphology/crystallinity and optimizing the interfacial carrier transport layer for efficient carrier kinetics.

4. Experimental Section

Materials and preparation: All chemicals were purchased from commercial suppliers as mentioned and unless otherwise specified, they were used as received. Caesium iodide (CsI, Sigma Aldrich, 99% purity), bismuth iodide (BiI_3, Sigma Aldrich, 99% purity) were purchased from as the mentioned company. We prepared 0.5 M precursor solutions ($CsBi_3I_{10}$ (CBI-1) and $Cs_3Bi_2I_9$ (CBI-2) by dissolving CsI and BiI3 powder at molar ratio of 1:3 and 3:2 in DMF and DMSO (7:3 (v:v)) at 70 ^{0}C for 12 hours. The BiI_3 precursor solution was prepared by dissolving 50-150 mg/mL in DMF at 70 ^{0}C for 12 hours in N_2-filled glovebox. [Poly(3,4-ethylenedioxythiophene):poly(styrene sulfonate) (PEDOT:PSS) (Clevios, Al4083) was diluted by mixing with methanol at ratio (3:7). The Poly [bis(4-phenyl)(2,4,6-trimethylphenyl)amine (PTAA) (0.5 wt%) and [6,6]-Phenyl C_{61} butyric acid methyl ester ($PC_{61}BM$) [Sigma Aldrich, 99% purity] solution (2 wt. %) were dissolved in anhydrous chlorobenzene (CB) at 50 ^{0}C for 7 hours. Aluminium doped zinc oxide (AZO) nanoparticle ink (Avantama, N-21X) was used. All the solutions were filtered using 0.45 μm syringe filters to avoid the risk of unwanted particles in the precursor solutions.

Device Fabrication: Solar cell devices were fabricated on pre-cleaned patterned indium tin oxide (ITO) coated glass substrates (15 Ω $square^{-1}$). The ITO substrates were pre-cleaned in an ultrasonic bath with detergent, pure water, and 2-propanol, followed by an ultraviolet-ozone

treatment for 5 min to remove the organic residuals. A thin PTAA HTM layer (~20 nm) was deposited onto ITO substrate by spin coating at 4000 rpm (2000 rpm/s speed) for 30 seconds and subsequently dried at 100 ℃ for 10 mins on a hot plate in a ambient nitrogen. Similarly, another thin HTM layer (~30 nm) (PEDOT:PSS) was deposited onto ITO substrate by spin coating at 3000 rpm for 30 seconds and subsequently dried at 130 ℃ for 30 min on a hot plate in ambient air. The NiOx (~30 nm) film was deposited by sputtering as mentioned in our earlier report. For the fabrication of Bi-based based thin film, the precursor solution (CsBI-1 or CsBI-2 or BiI_3) was spin coated at 1500 rpm for 20 s (ramping rate; 500 rpm/s) and 3000 rpm for 30 s. After spin coating, the films were crystallized by conventional annealing (CA) at various temperatures (90, 120, 150, 180, and 200 ℃) for 60 minutes. For antisolvent (AS) treated sample, the chlorobenzene of 150 μL was dripped after 20 s of the starting of spin coating annealed at 120 ℃ for 60 minutes. The solvent annealing of post antisolvent (AS) dripped samples was carried out putting about 5 μL of DMF on the edge of a cover glass at 120 ℃ for 60 minutes. For ETL, $PC_{61}BM$ was spun–coated on top of the Bi-HaP films at 800 rpm for 30 s coupled at 4000 rpm for 10 s annealed at 100 ℃ for 10 min. Then a thin electron selective layer (ESL); AZO layer was deposited by spinning at 2000 rpm for 20 s and dried it by annealing at 100 ℃ for 10 min. The device structure was completed by depositing thermally evaporated Ag of 100 nm at Ag at a pressure $<10^{-4}$ Pa. We sealed our devices of area ~0.26 cm^2 were using UV-curable resins.

Device Characterizations: The X-ray diffraction (XRD) patterns of fabricated films were collected using Bruker D8 advanced x-ray diffractometer (CuK_α radiation, λ= 1.54050 A). The morphology of films and cross-sectional images were taken by a high resolution scanning electron microscope (SEM) at 5 kV accelerating voltage (Hitachi, S-4800). The absorption spectra and photoluminescence (PL) spectra of various films were measured using UV-Vis-NIR spectrometer (7200, V-Jasco) and Spectrofluorometer (FP8500, Jasco), respectively.

Raman spectra were collected from micro Raman spectrometer (Horiba, green laser 532 nm). HOMO levels of transport layers were measured using a photoelectron spectrometer (Riken Keiki, AC-3). XPS spectra were collected using VersaProbe II (ULVAC-PHI, Japan). The current density–voltage (J-V) curves were measured with a scan rate of 0.05 V/s under 1 sun with an AM 1.5G spectral filter (100 $mWcm^{-2}$) coupled with an MPPT system (Systemhouse Sunrise Corp.). The external quantum efficiency (EQE) spectra were measured with a spectrometer (SM-250IQE, Bunkokeiki, Japan). Capacitance-frequency response (C-f) was measured with an LCR meter (E4980A, Agilent), which probes from 20 Hz to 2 MHz at ac voltage amplitude of 30 mV under dark condition. Then After conforming the geometric capacitance regime in c-f spectra), capacitance-voltage (C−V) measurements were carried out at 10 kHz (the geometric capacitance regime in C-f spectra).

Supporting Information

The Supporting Information is available free of charge on the website.

Photographs of CBI-1 and CBI-2 films, XRD patterns, Raman, PL spectra (90- 200 ℃); XRD of fresh and aged CBI-1 and CBI-2 films; XRD patterns of CBI-1and CBI-2 films prepared with CA, AS, and AS+SA methods; SEM images of CBI-1 films (CA, AS, and AS+SA); SEM image of BiI3 film and J-V characteristics, XPS spectra of the CBI-1 and CBI-2 films, Photoelectron spectra of plasma treated PTAA and NiOx.

Acknowledgements

The research was supported by the MEXT Program for Development of Environment Technology using Nanotechnology (GREEN), JSPS KAKENHI grant number JP16K06285. Dr. D. B. Khadka would like to acknowledge to International Center for Young Scientists (ICYS), NIMS for research funding.

REFERENCES

1 M. A. Green, Y. Hishikawa, E. D. Dunlop, D. H. Levi, J. Hohl-Ebinger and A. W. Y. Ho-Baillie, *Prog. Photovoltaics Res. Appl.*, 2018, **26**, 3–12.

2 R. Cheacharoen, N. Rolston, D. Harwood, K. A. Bush, R. H. Dauskardt and M. D. McGehee, *Energy Environ. Sci.*, 2018, **11**, 144–150.

3 Z. Wang, Q. Lin, F. P. Chmiel, N. Sakai, L. M. Herz and H. J. Snaith, *Nat. Energy*, 2017, **2**, 17135.

4 L. Liang and P. Gao, *Adv. Sci.*, 2018, 5, 1700331.

5 Z. Shi, J. Guo, Y. Chen, Q. Li, Y. Pan, H. Zhang, Y. Xia and W. Huang, *Adv. Mater.*, 2017, 29, 1605005.

6 Y. Rong, Y. Hu, A. Mei, H. Tan, M. I. Saidaminov, S. Il Seok, M. D. McGehee, E. H. Sargent and H. Han, *Science (80-.).*, 2018, **361**, eaat8235.

7 F. Hao, C. C. Stoumpos, D. H. Cao, R. P. H. Chang and M. G. Kanatzidis, *Nat. Photonics*, 2014, **8**, 489–494.

8 N. K. Noel, S. D. Stranks, A. Abate, C. Wehrenfennig, S. Guarnera, A.-A. Haghighirad, A. Sadhanala, G. E. Eperon, S. K. Pathak, M. B. Johnston, A. Petrozza, L. M. Herz and H. J. Snaith, *Energy Environ. Sci.*, 2014, **7**, 3061–3068.

9 N. K. Noel, S. D. Stranks, A. Abate, C. Wehrenfennig, S. Guarnera, A. Haghighirad, A. Sadhanala, G. E. Eperon, S. K. Pathak, M. B. Johnston, A. Petrozza, L. M. Herz and H. J. Snaith, *Energy Environ. Sci.*, 2014, **7**, 3061–3068.

10 W. Liao, D. Zhao, Y. Yu, C. R. Grice, C. Wang, A. J. Cimaroli, P. Schulz, W. Meng, K. Zhu, R. G. Xiong and Y. Yan, *Adv. Mater.*, 2016, **28**, 9333–9340.

11 I. Kopacic, B. Friesenbichler, S. F. Hoefler, B. Kunert, H. Plank, T. Rath and G. Trimmel, *ACS Appl. Energy Mater.*, 2018, **1**, acsaem.8b00007.

12 B. W. Park, B. Philippe, X. Zhang, H. Rensmo, G. Boschloo and E. M. J. Johansson, *Adv. Mater.*, 2015, **27**, 6806–6813.

13 M. B. Johansson, H. Zhu and E. M. J. Johansson, *J. Phys. Chem. Lett.*, 2016, **7**, 3467–3471.

14 M. Khazaee, K. Sardashti, J. P. Sun, H. Zhou, C. Clegg, I. G. Hill, J. L. Jones, D. C. Lupascu and D. B. Mitzi, *Chem. Mater.*, 2018, **30**, 3538–3544.

15 M. Abulikemu, S. Ould-Chikh, X. Miao, E. Alarousu, B. Murali, G. O. Ngongang Ndjawa, J. Barbé, A. El Labban, A. Amassian and S. Del Gobbo, *J. Mater. Chem. A*, 2016, **4**, 12504–12515.

16 T. Singh, A. Kulkarni, M. Ikegami and T. Miyasaka, *ACS Appl. Mater. Interfaces*, 2016, **8**, 14542–14547.

17 A. J. Lehner, D. H. Fabini, H. A. Evans, C. A. Hébert, S. R. Smock, J. Hu, H. Wang, J. W. Zwanziger, M. L. Chabinyc and R. Seshadri, *Chem. Mater.*, 2015, **27**, 7137–7148.

18 T. Baikie, S. Mhaisalkar, B. Ghosh, X. Guo, R. A. John, T. C. Sum, P. C. Harikesh, B. Wu, Arramel, C. Guet, N. Mathews and A. T. S. Wee, *Adv. Energy Mater.*, 2018, **8**, 1802051.

19 S. S. Shin, J. P. Correa Baena, R. C. Kurchin, A. Polizzotti, J. J. Yoo, S. Wieghold, M. G. Bawendi and T. Buonassisi, *Chem. Mater.*, 2018, **30**, 336–343.

20 S. S. Mali, H. Kim, D. H. Kim and C. Kook Hong, *ChemistrySelect*, 2017, **2**, 1578–1585.

21 J. P. Correa-Baena, L. Nienhaus, R. C. Kurchin, S. S. Shin, S. Wieghold, N. T. Putri Hartono, M. Layurova, N. D. Klein, J. R. Poindexter, A. Polizzotti, S. Sun, M. G. Bawendi and T. Buonassisi, *Chem. Mater.*, 2018, **30**, 3734–3742.

22 C. Ran, Z. Wu, J. Xi, F. Yuan, H. Dong, T. Lei, X. He and X. Hou, *J. Phys. Chem. Lett.*, 2017, **8**, 394–400.

23 F. Bai, Y. Hu, Y. Hu, T. Qiu, X. Miao and S. Zhang, *Sol. Energy Mater. Sol. Cells*, 2018, **184**, 15–21.

24 S. M. Jain, D. Phuyal, M. L. Davies, M. Li, B. Philippe, C. De Castro, Z. Qiu, J. Kim, T. Watson, W. C. Tsoi, O. Karis, H. Rensmo, G. Boschloo, T. Edvinsson and J. R. Durrant, *Nano Energy*, 2018, **49**, 614–624.

25 T. Singh, A. Kulkarni, M. Ikegami and T. Miyasaka, *ACS Appl. Mater. Interfaces*, 2016, **8**, 14542–14547.

26 S. Öz, J. C. Hebig, E. Jung, T. Singh, A. Lepcha, S. Olthof, F. Jan, Y. Gao, R. German, P. H. M. van Loosdrecht, K. Meerholz, T. Kirchartz and S. Mathur, *Sol. Energy Mater. Sol. Cells*, 2016, **158**, 195–201.

27 B. Yang, J. Chen, F. Hong, X. Mao, K. Zheng, S. Yang, Y. Li, T. Pullerits, W. Deng and K. Han, *Angew. Chemie - Int. Ed.*, 2017.

28 L. K. Ono, E. J. Juarez-Perez and Y. Qi, *ACS Appl. Mater. Interfaces*, 2017, 9, 30197–30246.

29 A. Nilă, M. Baibarac, A. Matea, R. Mitran and I. Baltog, *Phys. status solidi*, 2017, **254**, 1552805.

30 A. Saitoh, T. Komatsu, T. Karasawa, H. Ohtake and T. Suemoto, *Phys. status solidi*, 2001, **226**, 357–367.

31 D. Tiwari, D. Alibhai and D. J. Fermin, *ACS Energy Lett.*, 2018, **3**, 1882–1886.

32 J. Shin, M. Kim, S. Jung, C. S. Kim, J. Park, A. Song, K.-B. Chung, S.-H. Jin, J. H. Lee and M. Song, *Nano Res.*, 2018, **11**, 6283–6293.

33 G. Kieslich, S. Sun and A. K. Cheetham, *Chem. Sci.*, 2015, **6**, 3430–3433.

34 C. Ni, G. Hedley, J. Payne, V. Svrcek, C. McDonald, L. K. Jagadamma, P. Edwards, R. Martin, G. Jain, D. Carolan, D. Mariotti, P. Maguire, I. Samuel and J. Irvine, *Nat. Commun.*, 2017, **8**, 170.

35 U. H. Hamdeh, R. D. Nelson, B. J. Ryan, U. Bhattacharjee, J. W. Petrich and M. G. Panthani, *Chem. Mater.*, 2016, **28**, 6567–6574.

36 A. Kulkarni, T. Singh, M. Ikegami and T. Miyasaka, *RSC Adv.*, 2017, **7**, 9456–9460.

37 T. S. Sherkar, C. Momblona, L. Gil-Escrig, J. Ávila, M. Sessolo, H. J. Bolink and L. J. A. Koster, *ACS Energy Lett.*, 2017, **2**, 1214–1222.

38 D. B. Khadka, Y. Shirai, M. Yanagida, J. W. Ryan and K. Miyano, *J. Mater. Chem. C*, 2017, **5**, 8819–8827.

39 D. B. Khadka, Y. Shirai, M. Yanagida, T. Noda and K. Miyano, *ACS Appl. Mater. Interfaces*, 2018, **10**, 22074–22082.

40 S. Zhang, M. Stolterfoht, A. Armin, Q. Lin, F. Zu, J. Sobus, H. Jin, N. Koch, P. Meredith, P. L. Burn and D. Neher, *ACS Appl. Mater. Interfaces*, 2018, **10**, 21681–21687.

41 X. Xu, C. Ma, Y. Cheng, Y. M. Xie, X. Yi, B. Gautam, S. Chen, H. W. Li, C. S. Lee, F. So and S. W. Tsang, *J. Power Sources*, 2017, **360**, 157–165.

42 F. Qingxia, T. Xianglan, H. Bin, H. Ting, T. Licheng, C. Lie and C. Yiwang, *Adv. Sci.*,

2018, **0**, 1700387.

43 J. T. Heath, J. D. Cohen and W. N. Shafarman, *J. Appl. Phys.*, 2004, **95**, 1000–1010.

44 D. B. Khadka, Y. Shirai, M. Yanagida, T. Masuda and K. Miyano, *Sustain. Energy Fuels*, 2017, **1**, 755–766.

45 D. B. Khadka, Y. Shirai, M. Yanagida and K. Miyano, *ACS Appl. Mater. Interfaces*, 2019, acsami.8b20924.

46 M. Stolterfoht, C. M. Wolff, J. A. Márquez, S. Zhang, C. J. Hages, D. Rothhardt, S. Albrecht, P. L. Burn, P. Meredith, T. Unold and D. Neher, *Nat. Energy*, 2018, **3**, 847–854.

Table of Contents Graphics

The antisolvent treatment subsequent with solvent vapor annealing affected the morphology of caesium bismuth halide film and impacts on the device parameters tuning with the carrier transport layer.